ARTICLE

Intrinsic magnetic properties for $\mathrm{SmFe}_{12-x}T_x$ thin films via high-throughput experiments and machine learning techniques

Daisuke Ogawa[a], Ryotaro Akagi[a], Keitaro Sodeyama[a] and Yukiko K. Takahashi[a,b]

[a]National Institute for Materials Science, Tsukuba 305-0047, Japan
[b]RIEC Tohoku university, Sendai 980-0812, Japan

ARTICLE HISTORY
Compiled August 14, 2025

ABSTRACT

The development of next-generation permanent magnets has become critical due to the limited performance improvements in Nd-Fe-B magnets and concerns over rare earth supply. ThMn_{12}-type rare-earth intermetallic compounds have emerged as promising alternatives, offering superior performance and reduced rare earth content. This study systematically investigates the magnetic properties of $\mathrm{Sm}(\mathrm{Fe}_{12-x}T_x)$-based thin films synthesized via combinatorial sputtering. Various stabilizing elements (e.g., Ti, V, Co, Cr) were analyzed to explore their effects on phase stability, saturation magnetization ($\mu_0 M_s$), anisotropy field ($\mu_0 H_s$), and Curie temperature (T_c). High-throughput structural and magnetic characterizations, coupled with machine learning (ML) predictions, facilitated efficient data acquisition and analysis. Experimental results reaffirmed trends such as $\mu_0 M_s$ enhancement with Co and phase-stabilization capabilities of Ti and V. Novel insights into additives like Cr and Ta revealed potential T_c improvements. ML regression models (Random Forest and XGBoost) identified electronegativity as a key factor influencing $\mu_0 M_s$. Predictive analyses successfully estimated $\mu_0 M_s$ trends and ThMn_{12} phase stability for unexplored compositions, enhancing the active learning framework for material discovery. This work highlights the synergy of combinatorial deposition, high-throughput data collection, and ML-assisted prediction in accelerating the exploration of magnetic materials. Future extensions to multi-element systems and other magnetic phases are expected to expedite the discovery of high-performance magnets for motors and energy applications.

KEYWORDS

ThMn_{12}-based magnets, intrinsic magnetic properties, combinatorial sputtering, high-throughput experiment, machine learning

1. Introduction

Since the discovery in 1984 by Sagawa et al. [1], Nd-Fe-B magnets have been regarded as the highest-performing permanent magnets and are widely utilized in motors and generators. However, the potential of these magnets has been nearly exhausted, leaving limited room for performance improvement. Additionally, concerns over the stability of raw material supply, particularly the critical dependence on rare earth elements, have prompted the pursuit of next-generation permanent magnet materials, often referred to as post-neodymium magnets.

CONTACT D. Ogawa. Email: d.ogawa@shinetsu.jp
CONTACT Y. K. Takahashi. Email: TAKAHASHI.Yukiko@nims.go.jp

Among potential alternatives, the ThMn_{12}-type rare-earth intermetallics have attracted significant attention since the discovery of the SmTiFe_{11} alloy in 1987 by Ohashi et al. [2]. These 1-12 phase magnets are regarded as promising candidates due to several merits, such as reduced consumption of rare earth elements and favorable magnetic properties (e.g., saturation magnetization $\mu_0 M_s$, anisotropy field $\mu_0 H_s$, and Curie temperature T_c) [3]. Furthermore, a high thermal resistance is achieved, as evidenced by the retention of a coercivity ($\mu_0 H_c$) as high as 1 T even at an elevated temperature of 500 K without any heavy rare-earth addition[54]. Despite these advantages, the development of this magnetic system has faced major challenges since its early days, such as poor phase stability and the difficulty of suppressing secondary phases such as α-Fe, as well as the inability to achieve microstructures that are conducive to enhanced coercivity [4–8].

Initial stabilization efforts involved the use of substitutional elements like Ti or V to improve structural control, leading to moderately satisfactory magnetic properties [9, 10]. However, the performance of these magnets was still inferior to Nd-based magnets, which relegated their utility primarily to bonded magnet applications [11].

A resurgence in interest in ThMn_{12}-based rare-earth magnets arose in recent years when it was demonstrated that stabilizing elements could be significantly reduced or eliminated altogether using advanced thin-film processes [12] or through the introduction of Zr as an additive [13]. These breakthroughs highlighted the potential for ThMn_{12}-type magnets not only as a cost-effective alternative to Nd-Fe-B but also as a high-performance material capable of potentially surpassing $\mathrm{Nd}_2\mathrm{Fe}_{14}\mathrm{B}$ in magnetic properties. This development has prompted intensive research on both phase stability and coercivity enhancement in recent years.

Regarding phase stability, it has been demonstrated that adding Gd to rare-earth sites at partial stoichiometric levels (e.g., 0.2) prevents the formation of undesirable secondary phases like α-Fe and stabilizes the 1-12 phase [14]. Additionally, elements such as Ga and V were shown to enhance phase stability, whereas Cu did not demonstrate such effects [15]. Substituting Y at rare-earth sites has also been reported to decrease the average atomic radius and further stabilize the ThMn_{12} structure [16].

On the other hand, significant progress has been achieved in coercivity enhancement. Recent findings include identifying twinning inside the magnetic grains as a new contributor to coercivity reduction [17,22], advancements in strip-casting methods that employ Cu to suppress Fe concentration in the grain boundaries [19], and the utilization of Nb to improve amorphous phase formation and suppress α-Fe [20]. For sintered magnets envisioned for commercial applications, relatively high coercivities have been obtained, reaching 0.81 T for anisotropic $\mathrm{Sm(Fe,V)}_{12}$-based magnets [21] and 1.0 T for anisotropic $\mathrm{Sm(Fe,Ti,V)}_{12}$-based magnets [22]. Thin-film studies have shown particularly impressive results, with non-magnetic boundary layer control through additives such as B and Al, yielding record-high coercivity values of 1.87 T in the ThMn_{12} system [23].

Despite this progress, challenges persist, particularly in bulk magnet synthesis. Stabilizing elements such as Ti and V are still necessary, which imposes a trade-off between improving coercivity and maintaining high saturation magnetization. Although theoretical studies have evaluated the magnetic properties of various potential substituent elements [24–28], comprehensive experimental investigations remain sparse.

Recognizing these challenges, this study aims to address two key objectives. First, we aim to fabricate a wide range of ThMn_{12}-type thin films with systematic variations in additive elements and concentrations, thereby constructing a comprehensive high-throughput database of their magnetic properties ($\mu_0 M_s$, $\mu_0 H_s$, and T_c). Second, we intend to leverage machine-learning techniques to identify new additive elements that could enhance $\mu_0 M_s$.

The combinatorial sputtering method used in this study enables the efficient deposition of multiple compositions in a single experiment, facilitating high-throughput magnetic and structural analysis. Although this concept has been proposed since the 1960s [29], its integration with modern data analysis techniques, such as machine learning, has recently accelerated its adoption for material discovery [30–32].

By constructing a robust database and applying machine learning, this approach offers the potential to predict unexplored regions of additive element composition and concentration, thereby optimizing the design of master alloys for specific applications. Moreover, this methodology demonstrates the increasing importance of combining experimental and computational techniques in accelerating the discovery of next-generation functional materials.

2. Experimental details

2.1. Thin film preparation

The thin films of the Sm-Fe-T system were prepared using combinatorial sputtering techniques. The experimental setup, including the configuration of targets and substrate holders, is shown in Fig. 1. Sm, Fe, and additional target elements (denoted as T) were co-sputtered under stationary substrate conditions to introduce compositional gradients across the films. MgO(001) single-crystal substrates were used as the deposition base, while V was employed as the underlayer due to its well-known cubic crystal structure (bcc), which offers good lattice matching with the $\mathrm{ThMn_{12}}$-structured $\mathrm{SmFe_{12}}$ compound along its c-axis. The substrates were placed at positions No. 2, 5, 8, and 11 as indicated in Fig. 1(a). Both the underlayer and the main Sm-Fe-T layers were deposited at a substrate temperature of 400 °C. To prevent oxidation, a 10-nm-thick V capping layer was deposited on top of the Sm-Fe-T layer.

Various stabilizing elements T were introduced with the aim of stabilizing the $\mathrm{ThMn_{12}}$ structure by substituting Fe sites. These elements included metals previously known to stabilize the structure, such as Ti, V, Mo, W, Ta, Cr, Si, and Al [33], as well as experimentally less-explored elements Mn, Ni, Ru, Rh, and Pd.

2.2. Characterization

The elemental composition of the films was evaluated using X-ray fluorescence (XRF), specifically wavelength dispersive X-ray fluorescence (WDXRF). The elements, their corresponding fluorescence X-rays, and their peak positions used in the analysis are summarized in Supplementary Table S1. A monochromator-based diffraction mechanism was utilized to isolate the characteristic X-ray wavelengths, using Li(200), Pentaerythritol (PET), and Ge monochromators depending on the atomic numbers and fluorescence X-ray characteristics. It could be confirmed that the peak positions in the spectra did not overlap across the measured elements in Table S1.

The composition was estimated using the fundamental parameter (FP) method implemented in the measurement equipment's built-in software. The accuracy of compositional measurements depends on calibration, but based on 12-point measurements of identical samples, variations in x (for $\mathrm{Sm}_y\mathrm{Fe}_{12-x}T_x$) were within ±10%, while y values were within ±5%. These precision levels were sufficient to distinguish compositional variation induced by the combinatorial approach. However, for elements with high atomic numbers such as Ta or W, matrix effects became significant, necessitating careful interpretation of absolute compositional values.

The crystal structure of the films was examined using using a Smartlab (*Rigaku*) with Cu Kα radiation. Additionally, film thickness was measured using X-ray reflectometry (XRR) with approximately ±3% variation. All films used in this study have thicknesses in the range of 133–376 nm as decribed in Supplementary Table S3. These thicknesses are sufficiently large such that any phase boundary effects originating from the interface between the main layer and the underlayers can be safely neglected when evaluating the magnetic properties.

Saturation magnetization ($\mu_0 M_s$) was evaluated using a Vibrating Sample Magnetometer (VSM) using TM-VSM211483ASE (*Tamagawa*) capable of applying a maximum field of ±2.1 T and a Superconducting Quantum Interference Device (SQUID) using MPMS3 (*Quantum Design*) with a maximum field of ±7 T. The anisotropy field ($\mu_0 H_k$) was determined using the in-plane magnetization curve, measured with a Dynacool (*Quantum Design*) with 14 T maximum magnetic field, which was equipped with a large bore coil set in VSM mode. $\mu_0 H_k$ was obtained from the magnetic field value where easy-axis and hard-axis magnetization curves intersect by using a model that assumes an ideal single-domain, infinitely extended thin film, with the demagnetization correction coefficient for the in-plane direction $N_{//} = 0$.

The temperature dependence of magnetization (M-T curve) was measured using an oven-equipped SQUID-VSM (Quantum Design) over a temperature range of 300 K to 700 K. An external magnetic field of 0.5 T was applied during the measurement. The Curie temperature (T_c) was estimated by fitting the M-T curve using the Kuz'min formula [34].

Table 1 summarizes the throughput of the deposition and measurement steps. The use of the combinatorial sputtering method allowed for the simultaneous fabrication of four unique compositions in a single deposition run. High-throughput measurement systems were integrated wherever possible. XRF and VSM measurements utilized automatic sample exchangers, and the XRD system was equipped with automated multipoint measurement functions. However, $\mu_0 H_k$ measurements with the Dynacool system and T_c evaluations with SQUID-VSM required manual sample handling, limiting the throughput for those measurements.

2.3. Machine learning analysis

In the machine learning analysis, the input variable set (explanatory variables) consisted of elemental properties, including atomic number, atomic radius, ionization energy, electron affinity, electronegativity, ionic radius, period, and valence, to account for composition effects. The target variable was the experimentally obtained saturation magnetization ($\mu_0 M_s$), and "Generated Variable" as explained below. The compositional influence on each explanatory variable was calculated using a weighted sum, as shown in the example for Sample No. 1:

$$\begin{aligned}\text{Weighted Sum of Atomic Numbers for (Sample No. 1, Sm}_{9.08}\text{Fe}_{86.45}\text{Ti}_{4.46}\text{)} \\ = 9.08 \times 62 + 86.45 \times 26 + 4.46 \times 22 \\ = 2908.78\end{aligned} \tag{1}$$

This approach was applied to all descriptors. It should be noted here that the compositional analysis obtained from the experiments carries an uncertainty of up to 10%, which inevitably introduces a corresponding level of uncertainty into the calculated results. Two regression algorithms, Random Forest [35] and XGBoost [36], were employed for the data analysis. The exploration space for composition was defined as $\mathrm{Sm}_y\mathrm{Fe}_{12-x}T_x$ with $0 \leq x \leq 2$ and $0.8 \leq y \leq 2$. The candidate stabilizing elements T included a subset of 48 metallic elements excluding radioactive and toxic materials: Na, Mg, Si, Al, K, Ca, Sc, Ti, V, Cr, Mn, Co, Ni, Cu, Zn, Ga, Rb, Sr, Y, Zr, Nb, Mo, Ru, Rh, Pd, In, Sn, Cs, Ba, La, Ce, Pr, Nd, Pm, Eu, Gd, Tb, Dy, Ho, Er, Tm, Yb, Lu, Ta, W, Re, Pb, and Bi.

3. Results and Discussions

3.1. Combinatorial thin film synthesis

Fig. 2(a) shows the XRF spectrum of Sm-Fe-Ti thin film (Sample No. 1), with characteristic fluorescence peaks corresponding to Fe Kα, Sm Lα, and Ti Kα, observed using a LiF(200) monochromator. The composition analysis based on these peaks is shown in Fig. 2(b). By employing combinatorial deposition processes as detailed in Supplementary Table S2, eight compositions of $\mathrm{Sm}_y\mathrm{Fe}_{12-x}T_x$ films were synthesized and plotted as a function of y (vertical axis) and x (horizontal axis). Despite measurement errors, a compositional gradient trend was evident, demonstrating the effectiveness of the combinatorial technique.

XRD analyses verified the crystalline structural properties of the synthesized films. ThMn_{12} structures were successfully synthesized under specific elemental compositions and concentrations, while other conditions failed to yield this structure. For example, Fig. 3(a) presents the XRD pattern (out-of-plane) for SmFeTi (Sample No. 1), showcasing peaks attributed to the (002) and (004) planes of the ThMn_{12} structure at approximately 37 ° and 79 °, respectively. The inset of Fig. 3(a) highlights the (044) peak obtained through fine angular adjustment, enabling the determination of lattice constants (a = 0.8476 nm, c = 0.4847 nm), which are in close agreement with reported literature values. A small intensity signal near 60 ° and 65 ° corresponds to bcc-structured V and Fe, respectively, likely present beneath the SmFeTi main phase, though weak peak of α-Fe intensities suggest minimal influence on the magnetic properties.

Conversely, Fig. 3(b) demonstrates XRD data for SmFeV (Sample No. 15), where the absence of peaks corresponding to ThMn_{12} indicates structural failure. In this study, samples with a successfully formed ThMn_{12} phase were labeled as "Generated = 1," while unsuccessful samples were labeled as "Generated = 0." The degree of ThMn_{12} phase formation was further quantified as the "Degree of Generating," calculated using the following expression:

$$\text{Degree of Generating} = \exp(\alpha), \tag{2}$$

Here, α represents the slope obtained from a linear fit of Generated versus x (additive concentration), fixing the intercept at (0,1). Though rough estimates due to limited trials and thin-film-specific conditions, this parameter provides an approximate indication of phase stability trends for additives. For instance, Sm-Fe-Cr exhibited Degree of Generating = 0.8, while Sm-Fe-Mn showed a lower value of 0.4 shown in Fig. 3(c)

3.2. Magnetic properties with various additives

Fig. 4(a) presents magnetic hysteresis loops of Sm-Fe-Ti (Sample No. 1) measured with magnetic field directions both along and perpendicular to the film plane. Strong perpendicular magnetic anisotropy is clearly seen from the results, which also enabled estimation of the saturation magnetization $\mu_0 M_s$ and the anisotropy field $\mu_0 H_k$. Fig. 4(b) shows the magnetization as a function of temperature (M-T curve) of Sm-Fe-Ti, where fitting with the Kuz'min's function revealed a Curie temperature of T_c = 563.5 K, consistent with reported literature. The deviations from the Kuz'min fits near T_c may be attributed to the external magnetic field of 0.5 T that was applied during the measurements.

From these measurements, all samples obtained in this experiment: power input for sputtering, position during deposition, composition, presence of $\mathrm{ThMn_{12}}$ structure formation (Generated), film thickness evaluated by XRR for $\mathrm{Sm}_y\mathrm{Fe}_{12-x}T_x$ (T=Ti, V, Mo, W, Ta, Cr, Si, Al, Mn, Ni, Ru, Rh, Pd), The lattice constants a and c evaluated by XRD, $\mu_0 M_s$[T] evaluated by VSM, T_c[K] evaluated by SQUID-VSM, and $\mu_0 H_k$[T] evaluated by dynacool are summarized in Table S3 in the Supplimentary.

As shown in Fig. 5(a), the saturation magnetization $\mu_0 M_s$ for T = Mo, Ti, and Cr decreases with increasing concentration x. Literature values for Co are also plotted for comparison [37–39].

For T=Mo, Ti, and Cr, $\mu_0 M_s$ decreases with increasing x and increases for Co. The concentration dependence of $\mu_0 M_s$ for each added element was linearly fitted and the slope was defined to ΔM_s.

This trend of $\mu_0 M_s$ reduction by Ti addition is consistent with previous reports [40,41], and the different reduction rates depending on the element cannot be explained by a simple dilution effect of the added element [42], but may instead arise from site-specific substitutions [43,44] and element-specific interactions [40,45,46].

The internal magnetic field of Fe sites varies by site, following the order $8i > 8j > 8f$ [3,38,47]. Stabilizing elements such as Ti and V are primarily substituted at the Fe(8i) site [40,48–50]. In contrast, Si are predominantly substituted at the Fe(8f) site [44]. Furthermore, Co shows preferential substitution depending on the Sm concentration, either at the Fe(8f) site or the Fe(8j) site [51,52]. It has also been reported that Ti has a magnetic moment within the $\mathrm{ThMn_{12}}$ structure, which is antiferromagnetically coupled to Fe and Co [53]. These factors may contribute to the cause of different ΔM_s values for different additive elements.

Fig. 5(b) shows the results of ΔM_s plotted as a degree of generating for the various added elements. In the experimental results, only Co has the positive ΔM_s. This is attributed to the increase in internal magnetic field due to Co addition [38,47].

Cr, Ta, Al, and Ti have relatively small reduction rate. On the other hand, focusing on the degree of generating, Ti, V, and Cr tended to generate $\mathrm{ThMn_{12}}$ easily, while Al and Si were less likely to generate it. As for Al, this corresponds to the literature [54] that $\mathrm{Sm(Fe_{0.8}Co_{0.2})_{12}}$ does not diffuse into the crystal.

Fig. 5(c) shows the results of ΔH_k plotted in Degree of generating for various added elements, showing that Co and V tend to keep $\mu_0 H_s$ relatively well, consistent with previous literature [37,55,56].

It has been theoretically argued that $\mu_0 H_k$ varies with the type of element, such as Ti or V, due to the electron-cloud distortion attracting the prolate Sm 4f orbitals to the screened nuclear charges of surrounding ligands [57], and, in particular, it has been discussed that in the region from room temperature to high temperatures, the 4f–3d exchange coupling (J_{RT}) between rare earth elements and Fe becomes dominant [59]. So far, no additive elements have been found to increase $\mu_0 H_k$. The theory predicts that $\mu_0 H_k$ would be increased if Ti or V were substituted at the 4f site [57], but in practice, $\mu_0 H_k$ has not increased, possibly because Ti and V have been substituted at the 8i site.

Fig. 5(d) shows the results of ΔT_c plotted by Degree of generating for various added elements, where T_c increased for T=Co, Si, V, Cr, and for T=Ta. Ti, T_c maintained almost the same value with addition.

The maintenance of T_c by the addition of Ti and the increase in T_c by the addition of V, Cr, and Co are consistent with the literature [26,56,58]. In these references, it is argued that small amounts of Cr or V additions increase T_c due to enhanced Fe-V or Fe-Cr exchange interactions and enhanced surrounding Fe-Fe exchange interactions. In addition, the results of this experiment, in which T_c is significantly reduced by Al addition, are consistent with previous literature [60].

These graphs of Degree of generating dependence of ΔM_s, ΔH_k, and ΔT_c show again that Co, Ti, V, and Cr, which are commonly used in this system, are excellent additive elements in terms of intringent magnetic properties.

On the other hand, another objective of this paper is not only to build a database but also to use machine learning to predict additional elements and concentrations in untested areas. Therefore, we analyzed all experimental data, including both favorable and unfavorable results, and the prediction outcomes will be presented in the next section.

3.3. Machine learning analyses

Table 2 summarizes the details of each analysis attempt, including the number of samples used for analysis in each trial, the types of additional elements, and the R^2, MAE, and RMSE values obtained from the Random Forest regression and XGBoost analyses.

Data from samples that did not generate 1-12 (Generated=1) were excluded from this analysis.

Both models exhibit a clear trend in which the coefficient of determination (R^2) increases as the amount of data increases, indicating that the accuracy of the models improves with more data. On the other hand, the error metrics (MAE and RMSE) remain nearly constant or even increase slightly, suggesting that the precision of the analysis does not improve as the dataset grows.

Fig. 6(a) presents a heatmap illustrating the relationship between each descriptors (Atomic number, Period, Atomic radius, Electronegativity, Electron affinity, Ion radius, Valence, and Ionization energy) and the target variable $\mu_0 M_s$ in the 5th Random Forest Regression analysis.

Fig. 6(b) shows a scatter plot of the experimental values versus the predicted values. The closer the data points are to the straight line, the better the agreement between the experimental and predicted values, providing a visual representation of the level of accuracy.

Fig. 6(c) displays the importance parameters estimated through cross-validation using the trained model. The differences between these results and the heatmap in Fig. 6(a) arise from the non-linear nature of the relationships between the descriptors (related to the specified elemental information) and the target variable $\mu_0 M_s$. These relationships are not simple one-to-one linear correlations but involve complex interactions. The use of Random Forest regression confirms that this non-linearity is appropriately considered in the analysis. The result of analysis shows a strong negative linear correlation is observed between the atomic radius and $\mu_0 M_s$, which indicate that $\mu_0 M_s$ decreases as atomic radius increases. On the other hand, although electronegativity does not show a simple strong linear correlation with $\mu_0 M_s$ in Fig. 6(a), electronegativity emerges as the most influential parameter for predicting $\mu_0 M_s$ according to the feature importance analysis in Fig. 6(c). This suggests that while the direct linear relationship between electronegativity and $\mu_0 M_s$ is small, electronegativity may have a significant nonlinear or synergistic effect—possibly involving complex interplay with other features—that strongly affects saturation magnetization. Overall, the data analysis demonstrates that atomic radius acts as a linearly correlated descriptor, whereas electronegativity plays a key, but more intricate, role in determining $\mu_0 M_s$ within this material system.

Fig. 7(a) compares the experimental and predicted saturation magnetization ($\mu_0 M_s$) for T = Ti and Co as a function of the additional element concentration, plotted on the horizontal axis. The predictions combine the results from the 1st, 2nd, and 3rd trials. In the figure, ΔM_{exp} represents the slope obtained from linear fitting of the experimental data, while $\Delta M_{1stpred.}$, $\Delta M_{2ndpred.}$, $\Delta M_{3rdpred.}$ indicate the slopes obtained from linear fitting of the predicted results from the 1st, 2nd, and 3rd trials, respectively. For both Ti and Co, it can be observed that as the number of prediction trials increases, the ΔM_s values, which correspond to the change in $\mu_0 M_s$, become closer to the experimental values.

Fig. 7(b) shows a plot comparing ΔM_{exp} for each additive element with $\Delta M_{3rdpred.}$ from the third analysis. While the absolute values do not always match perfectly, the overall trends in the changes are generally consistent.

In active learning that involves iterative experimentation and prediction, it is not sufficient to select candidates for the next experiment solely based on additive elements predicted to yield high $\mu_0 M_s$. By also predicting parameters related to phase formation (Generated), it becomes possible to select experimental candidates that balance high $\mu_0 M_s$ with a high probability of forming the $\mathrm{ThMn_{12}}$ phase. This approach can reduce unnecessary work and improve the efficiency of material exploration.

Fig. 8(a) shows heatmaps of the experimental and predicted Generated values estimated using two algorithms: Random Forest and XGBoost. A Generated value of "1" indicates that the $\mathrm{ThMn_{12}}$ structure is "formed," while "0" indicates it is "not formed." Regions where both the experimental and predicted values are "0" or both are "1" represent agreement between experiment and prediction. The critical regions are where the prediction is "1" but the experimental value is "0," or the prediction is "0" but the experimental value is "1." These cases suggest the potential for unnecessary experiments or missed opportunities to identify $\mathrm{ThMn_{12}}$ structures. However, since the mean accuracy is 0.71 for Random Forest and 0.75 for XGBoost, using this analysis is more efficient than not using it at all. In additon, the "recall" value, which is the success rate of predictions for experimentally accessible cases, is 0.92 for Random Forest and 0.86 for XGBoost. It indicates that it is worth to conduct experiments based on the predictions for the $\mathrm{ThMn_{12}}$ structure formation.

Fig. 8(b) plots the $\Delta M_{3rdpred.}$ values of all the elements used in the exploration, along with their corresponding predicted generating ratios, arranged in descending order of $\Delta M_{3rdpred.}$. This study employs a data-driven approach, where machine learning predictions are based on experimental results. Interestingly, first-principles calculations have also shown that substituting light transition metals (Ti, V, Cr, Mn) significantly reduces the magnetic moment of $\mathrm{NdFe}_{11}T$, while substituting heavy transition metals (Co, Ni, Cu, Zn) tends to increase it [25]. Additionally, active learning methods that combine first-principles calculations with machine learning suggest a slight increase in $\mu_0 M_s$ for $\mathrm{SmFe}_{11}X$ when X = Cu or Zn [28]. Even though the phase stability of the ThMn_{12} structure was not taken into account to $\mu_0 M_s$ in either our prediction, or previous first-principles calculations [25], it is significant that these independent methods consistently indicate that not only Co but also Ni and Cu substitutions increase $\mu_0 M_s$. This agreement across different approaches suggests that the observed trends would be robust and that the employed methods could be trusted as reliable tools for the design of new magnetic materials.

4. Conclusion

This study has successfully established a comprehensive combinatorial dataset for the $\mathrm{SmFe}_{12-x}\mathrm{T}_x$ magnet system, comprising compositional, structural, and magnetic properties. Reproduction of known trends, such as the effects of Co, Ti, and V on $\mu_0 M_s$, $\mu_0 H_s$, and T_c, validates the experimental and analytical approaches, while new insights were gained regarding Cr, Ta, and Si as potential candidates for enhancing T_c. Furthermore, our machine learning analysis revealed that the reduction rate of saturation magnetization ($\mu_0 M_s$) caused by Cr substitution is relatively small, and that Ni and Cu are predicted to increase $\mu_0 M_s$, suggesting their potential as beneficial dopants for magnetic performance optimization.

The first key contribution of this work is a demonstration of the combinatorial synthesis and high-throughput characterization approach, enabling efficient data collection spanning multiple additive types and concentrations. By utilizing machine learning algorithms, the second major contribution lies in the identification of crucial parameters (e.g., electronegativity) that influence $\mu_0 M_s$ and the prediction of ThMn_{12} phase stability. Despite limitations such as a focus on single-element substitutions in Fe sites, the machine-learning framework developed here is expandable to multi-element substitutions and other magnetic systems, including TbCu_7-type alloys reported to reach $\mu_0 H_k$ values above 20 T [61].

These findings underscore the power of integrating high-throughput experimentation with predictive learning (active learning), creating a foundation for accelerated discovery of high-performance magnetic materials. Moving forward, this methodology is expected to contribute significantly to the efficient exploration of next-generation permanent magnets.

Acknowledgments

The authors thank T. Hiroto for their assistance with the use of the experiment machines. The authors thank A. Nakama for their assistance with the deposition of films. This work was supported in part by the JST CREST program (Grant No. JPMJC22C3) and MEXT program "Data Creation and Utilization-Type Material Research and Development Project" (Grant No. JPMXP1122715503). This research was conducted in part using the Research Data Express (RDE) provided by the Materials Data Platform (MDPF) of the National Institute for Materials Science (NIMS).

References

[1] Sagawa M, Fujimura S, Togawa N, et al. New material for permanent magnets on a base of Nd and Fe. J Appl. Phys. 1984;55:2083–2087.

[2] Ohashi K, Yokoyama T, Osugi R, et al. The magnetic and structural properties of R-Ti-Fe ternary compounds. IEEE Trans. Magn. 1987;23:3101–3103.

[3] Hu BP, Li HS, Gavigan JP, et al. Intrinsic magnetic properties of the iron-rich $ThMn_{12}$-structure alloys $R(Fe_{11}Ti)$; R=Y, Nd, Sm, Gd, Tb, Dy, Ho, Er, Tm and Lu. J. Phys.: Condens. Matter 1989;1:755–770.

[4] Schultz L, Wecker J. Coercivity in $ThMn_{12}$-type magnets. J Appl. Phys. 1988;64:5711–5713.

[5] Singleton EW, Strzeszewski J, Hadjipanayis GC. Magnetic and structural properties of melt-spun rare-earth transition-metal intermetallics with $ThMn_{12}$ structure. J Appl. Phys. 1988;64:5717–5719.

[6] Cochet-Muchy D, Païdassi S. Rapidly quenched hard magnetic alloys with $ThMn_{12}$-type structure. J. Magn. Magn. Mater. 1990;83:249–250.

[7] Ding J, Rosenberg M. Magnetic hardening of melt-spun and crystallized Sm-Fe-V and Sm-(Fe, Co)-V alloys. J. Less-Common Met. 1990;161:369–374.

[8] Xiao QF, Sun XK, Geng DY, et al. Structure and magnetic properties of rapidly quenched Sm-Fe-Ti alloys. J. Magn. Magn. Mater. 1995;140–144:1093–1094.

[9] Okada M, Kojima A, Yamagishi K, et al. High coercivity in melt-spun $SmFe_{10}(Ti, M)_2$ ribbons (M=V/Cr/Mn/Mo). IEEE Trans. Magn. 1990;26:1376–1378.

[10] Schultz L, Schnitzke K, Wecker J. High coercivity in mechanically alloyed Sm-Fe-V magnets with a $ThMn_{12}$ crystal structure. Appl. Phys. Lett. 1990;56:868–870.

[11] Suzuki S, Inoue N, Miura T. Magnetic properties of $RFe_{11-x}Co_xTiN_y$ (R:Nd, Pr) compounds with $ThMn_{12}$ type structure. IEEE Trans. Magn. 1992;28:2005–2009.

[12] Hirayama Y, Takahashi YK, Hirosawa S, et al. $NdFe_{12}N$ hard-magnetic compound with high magnetization and anisotropy field. Scr. Mater. 2015;95:70–72.

[13] Kuno T, Suzuki S, Urushibata K, et al. (Sm, Zr)(Fe, Co)$_{11.0-11.5}$Ti$_{1.0-0.5}$ compounds as new permanent magnet materials. AIP Adv. 2016;6:025221.

[14] Tozman P, Sepehri-Amin H, Ohkubo T, et al. Intrinsic magnetic properties of (Sm, Gd)Fe_{12}-based compounds with minimized addition of Ti. J. Alloys Compd. 2021;855:157491.

[15] Dirba I, Harashima Y, Sepehri-Amin H, et al. Thermal decomposition of $ThMn_{12}$-type phase and its optimum stabilizing elements in $SmFe_{12}$-based alloys. J. Alloys Compd. 2020;813:152224.

[16] Hagiwara M, Sanada N, Sakurada S. Effect of Y substitution on the structural and magnetic properties of $Sm(Fe_{0.8}Co_{0.2})_{11.4}Ti_{0.6}$. J. Magn. Magn. Mater. 2018;465:554–558.

[17] Ener S, Skokov KP, Palanisamy D, et al. Twins – a weak link in the magnetic hardening of $ThMn_{12}$-type permanent magnets. Acta Mater. 2021;214:116968.

[18] Zhang JS, Tang X, Bolyachkin A, et al. Microstructure and extrinsic magnetic properties of anisotropic Sm(Fe, Ti, V)$_{12}$-based sintered magnets. Acta Mater. 2022;238:118228.

[19] Srinithi AK, Tang X, Sepehri-Amin H, et al. High-coercivity $SmFe_{12}$-based anisotropic sintered magnets by Cu addition. Acta Mater. 2023;256:119111.

[20] Zhou TH, Qia HD, Lim JT, et al. Effects of Ti–V pair substitution and grain boundary modification on physical and magnetic properties of $Sm(Fe_{0.8}Co_{0.2})_{12}$ bulk magnet. J. Alloys Compd. 2023;966:171620.

[21] Otsuka K, Kamata M, Nomura T, et al. Coercivities of Sm-Fe-M Sintered Magnets with $ThMn_{12}$-Type Structure (M=Ti, V). Mater. Trans. 2021;62:887–891.

[22] Zhang JS, Tang X, Bolyachkin A, et al. Microstructure and extrinsic magnetic properties of anistropic Sm(Fe,Ti,V)$_{12}$-based sintered magnet. Acta Mater. 2022;238:118228.

[23] Mori Y, Nakatsuka S, Hatanaka S, et al. Enhancement of coercivity for Sm(Fe-Co)$_{12}$-B thin films by introduction of Sm seed layer. J Magn Soc Jpn. 2024;48:17–20.

[24] Harashima Y, Terakura K, Kino H, et al. First-principles study of structural and mag-

netic properties of R(Fe, Ti)$_{12}$ and R(Fe, Ti)$_{12}$N (R = Nd, Sm, Y). JPS Conf. Proc. 2015;5:011021.

[25] Harashima Y, Terakura K, Kino H, et al. First-principles study on stability and magnetism of NdFe$_{11}$M and NdFe$_{11}$MN for M = Ti, V, Cr, Mn, Fe, Co, Ni, Cu, Zn. J Appl. Phys. 2016;120:203904.

[26] Fukazawa T, Akai H, Harashima Y, et al. First-principles investigation of Nd(Fe, M)$_{12}$(M = K–Br) and Nd(Fe, Cr, Co, Ni, Ge, As)$_{12}$: possible enhancers of Curie temperature for NdFe$_{12}$ magnetic compounds. Acta Mater. 2022;226:117597.

[27] Körner W, Krugel G, Elsässer C, et al. Theoretical screening of intermetallic ThMn$_{12}$-type phases for new hard-magnetic compounds with low rare earth content. Sci. Rep. 2016;6:24686.

[28] Nguyen D-N, Kino H, Miyake T, et al. Explainable active learning in investigating structure-stability of SmFe$_{12-\alpha-\beta}$X$_\alpha$Y$_\beta$ structures X, Y = Mo, Zn, Co, Cu, Ti, Al, Ga. MRS Bull. 2022;48:31–44.

[29] Kennedy K, Stefansky T, Davy G, et al. Rapid method for determining ternary-alloy phase diagrams. J Appl. Phys. 1965;36:3808–3810.

[30] Hong Y, de Moraes I, Eslava GG, et al. A high throughput study of both compositionally graded and homogeneous Fe–Pt thin films. J Mater Res Technol. 2022;18:1245–1255.

[31] Kovacs A, Fischbacher J, Oezelt H, et al. Physics-informed machine learning combining experiment and simulation for the design of neodymium-iron-boron permanent magnets with reduced critical-elements content. Front. Mater. 2023;9:1094055.

[32] Dilipan AR, Sepehri-Amin H, Modak R, et al. Combinatorial sputtering synthesis of TbCu$_7$-type Sm-Fe based compounds: a study on phase, composition, and extrinsic magnetic properties. J. Alloys Compd. 2025;1010:177723.

[33] De Mooij DB, Buschow KHJ. Some novel ternary ThMn$_{12}$-type compounds. J. Less-Common Met. 1988;136:207–215.

[34] Kuz'min MD. Shape of Temperature Dependence of Spontaneous Magnetization of Ferromagnets: Quantitative Analysis. Phys. Rev. Lett. 2005;94:107204.

[35] Breiman L. Random Forests. Mach. Learn. 2001;45:5–32.

[36] Chen T, Guestrin C. XGBoost: A Scalable Tree Boosting System. arXiv. 2016;arXiv:1603.02754.

[37] Hirayama Y, Takahashi YK, Hirosawa S, et al. Intrinsic hard magnetic properties of Sm(Fe$_{1-x}$Co$_x$)$_{12}$ compound with the ThMn$_{12}$ structure. Scr. Mater. 2017;138:62–65.

[38] Ogawa D, Fukazawa T, Li S, et al. Temperature dependence of site-resolved Fe magnetic moments in ThMn$_{12}$-type Sm(Fe$_{0.8}$Co$_{0.2}$)$_{12}$ compounds studied via synchrotron Mössbauer spectroscopy. J. Magn. Magn. Mater. 2022;552:169188.

[39] Kobayashi S, Ogawa D, Xu XD, et al. Multimodal analysis of Zr substitution effects on magnetic and crystallographic properties in (Sm$_{1-x}$Zr$_x$)(Fe$_{0.8}$Co$_{0.2}$)$_{12}$ compounds with ThMn$_{12}$ structure. Acta Mater. 2023;242:118454.

[40] Coehoorn R. Electronic structure and magnetism of transition-metal-stabilized YFe$_{12-x}$M$_x$ intermetallic compounds. Phys. Rev. B. 1990;41:11790–11797.

[41] Makurenkova A, Ogawa D, Tozman P, et al. Intrinsic hard magnetic properties of Sm(Fe, Co)$_{12-x}$Ti$_x$ compound with ThMn$_{12}$ structure. J. Alloys Compd. 2021;861:158477.

[42] Yang H, Li QA, Tang N, et al. Magnetic properties of RFe$_{12-x}$V$_x$ (R = Y, Nd) compounds. J. Magn. Magn. Mater. 1993;123:317–319.

[43] Denissen CJM, Coehoorn R, Buschow KHJ. ^{57}Fe Mössbauer study of RFe$_{12-x}$T$_x$ compounds (T = V, Cr, Mo). J. Magn. Magn. Mater. 1990;87:51–56.

[44] Sun G, Chen B, Du H, et al. Electronic structure and magnetism of R(Fe, Si)$_{12}$ (R = Y, Nd). Sci. China, Ser. G 2006;49:195–202.

[45] Ohashi K, Tawara Y, Osugi R, et al. Magnetic properties of Fe-rich rare-earth intermetallic compounds with a ThMn$_{12}$ structure. J Appl. Phys. 1988;64:5714–5716.

[46] Verhoef R, de Boer FR, Zhang ZD, et al. Moment reduction in RFe$_{12-x}$T$_x$ compounds (R = Gd, Y and T = Ti, Cr, V, Mo, W). J. Magn. Magn. Mater. 1988;75:319–322.

[47] Kobayashi K, Suzuki S, Kuno T, et al. The origin of high magnetic properties in (R,

Zr)(Fe, Co)$_{11.0-11.5}$Ti$_{1.0-0.5}$N$_y$ (y = 1.0–1.4 for R = Nd, y = 0 for R = Sm) compounds. J. Magn. Magn. Mater. 2017;426:273–278.

[48] Solzi M, Pareti L, Moze O, et al. Magnetic anisotropy and crystal structure of intermetallic compounds of the ThMn$_{12}$ structure. J Appl. Phys. 1988;64:5084–5087.

[49] Yang Y, Sun H, Kong L, et al. Neutron diffraction study of Y(Ti, Fe)$_{12}$. J Appl. Phys. 1988;64:5968–5970.

[50] Sinnemann T, Rosenberg M, Buschow KHJ. Mössbauer spectroscopy study of RFe$_{12-x}$V$_x$ intermetallics. J. Less-Common Met. 1989;146:223–228.

[51] Martin-Cid A, Salazar D, Schönhöbel AM, et al. Magnetic properties and phase stability of tetragonal Ce$_{1-x}$SmxFe$_9$Co$_2$Ti 1:12 phase for permanent magnets. J. Alloys Compd. 2018;749:640–644.

[52] Kobayashi K, Suzuki S, Kuno T, et al. The stability of newly developed (R, Zr)(Fe, Co)$_{12-x}$Ti$_x$ alloys for permanent magnets. J. Alloys Compd. 2017;694:914–920.

[53] Suzuki H, Nambu A, Okamoto M, et al. X-ray magnetic circular dichroism and neutron diffraction measurements of the magnetic moment of titanium in Sm(Fe$_{0.8}$Co$_{0.2}$)$_{11}$Ti. Phys. Rev. B. 2019;100:144443.

[54] Sepehri-Amin H, Kulesh N, Mori Y, et al. Microstructure and coercivity of Al-diffused Sm(Fe, Co, B)$_{12}$ film. Scr. Mater. 2024;242:115955.

[55] Ogawa D, Yoshioka T, Xu XD, et al. Magnetic anisotropy constants of ThMn$_{12}$-type Sm(Fe$_{1-x}$Co$_x$)$_{12}$ compounds and their temperature dependence. J. Magn. Magn. Mater. 2020;497:165965.

[56] Tozman P, Fukazawa T, Ogawa D, et al. Peculiar behavior of V on the Curie temperature and anisotropy field of SmFe$_{12-x}$V$_x$ compounds. Acta Mater. 2022;232:117928.

[57] Yoshioka T, Tsuchiura H, Novák P, et al. Effect of element doping and substitution on the electronic structure and macroscopic magnetic properties of SmFe$_{12}$-based compounds. Phys. Rev. B. 2022;105:014402.

[58] Fukazawa T, Akai H, Harashima Y, et al. First-principles study of intersite magnetic couplings and Curie temperature in RFe$_{12-x}$Cr$_x$ (R = Y, Nd, Sm). J Phys Soc Jpn. 2018;87:044706.

[59] Matsumoto M, Akai H, Doi S, et al. Relevance of 4f-3d exchange to finite-temperature magnetism of rare-earth permanent magnets: An ab-initio-based spin model approach for NdFe$_{12}$N. J Appl. Phys. 2016;119:213901.

[60] Simon D, Wuest H, Koehler T, et al. The quaternary system Sm-Fe-Mo-Al and the effect of Al substitution on magnetic and structural properties of its ThMn$_{12}$ phase. J. Alloys Compd. 2019;770:301–307.

[61] Dilipan AR, Ogawa D, Sepehri-Amin H, et al. Excellent intrinsic magnetic properties in the TbCu$_7$-type Sm-Fe-N compound. Acta Mater. 2024;274:119996.

Table 1.: Throughputs of each process evaluated with different methods.

each process		Method	Throughput
Fabrication		Combinatorial sputtering system	high
Characterization	composition	Auto-sample-exchange XRF	high
	crystal structure	Automatic multi-point XRD	high
	Thickness	Automatic multi-point XRR	high
	$\mu_0 M_s$	Auto-sample-exchange VSM	high
	T_c	Manual-sample-exchange SQUID	Low
	$\mu_0 H_s$	Manual-sample-exchange PPMS	Low

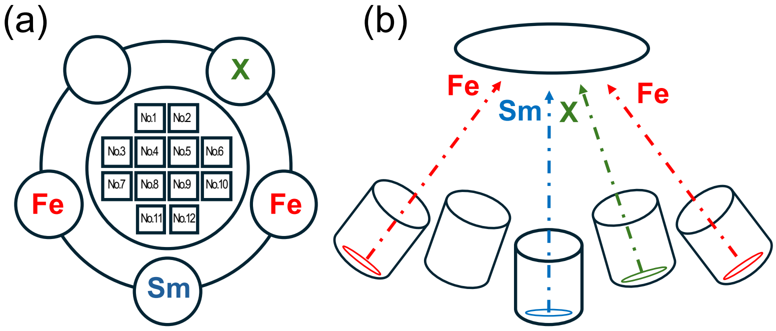

Figure 1.: (a) Target configuration and substrate location in the sputtering chamber. (b) Schematic of the cathode and substrate from the side.

Table 2.: Summary of analysis details, including the number of samples used in each trial, types of added elements, and evaluation metrics (R^2, MAE, and RMSE) obtained from Random Forest regression and XGBoost analyses.

	number of dataset	additive elements	Random Forest			XGBoost		
			R^2	MAE	RMSE	R^2	MAE	RMSE
1st	30	Ti, V, Mo, W, Ta	0.5	0.042	0.004	0.520	0.045	0.004
2nd	53	above+Cr, Si, Al, NA	0.46	0.06	0.006	0.503	0.057	0.006
3rd	68	above+Co	0.636	0.118	0.028	0.700	0.104	0.023
4th	76	above+Ni, Mn, Ru	0.651	0.08	0.014	0.602	0.085	0.016
5th	88	above+Rh, Pd	0.723	0.088	0.013	0.707	0.086	0.013

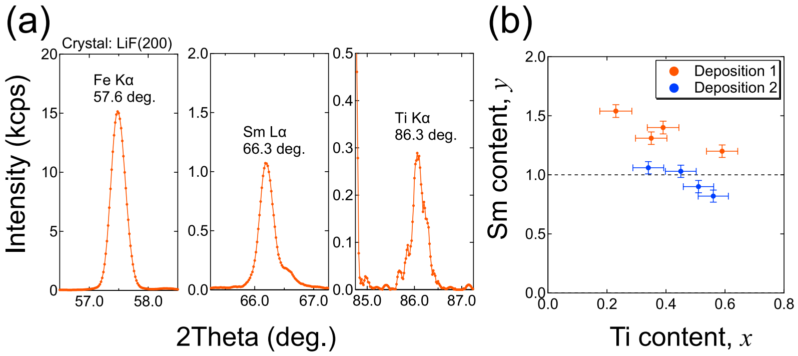

Figure 2.: (a) XRF spectrum of SmFeTi thin film (Sample No. 1), showing characteristic fluorescence peaks corresponding to Fe Kα, Sm Lα, and Ti Kα, obtained using a LiF(200) monochromator. (b) Composition analysis of SmyFe$_{12-x}T_x$ films synthesized via combinatorial deposition processes (detailed in Supplementary Table S2), plotted as a function of y (vertical axis) and x (horizontal axis).

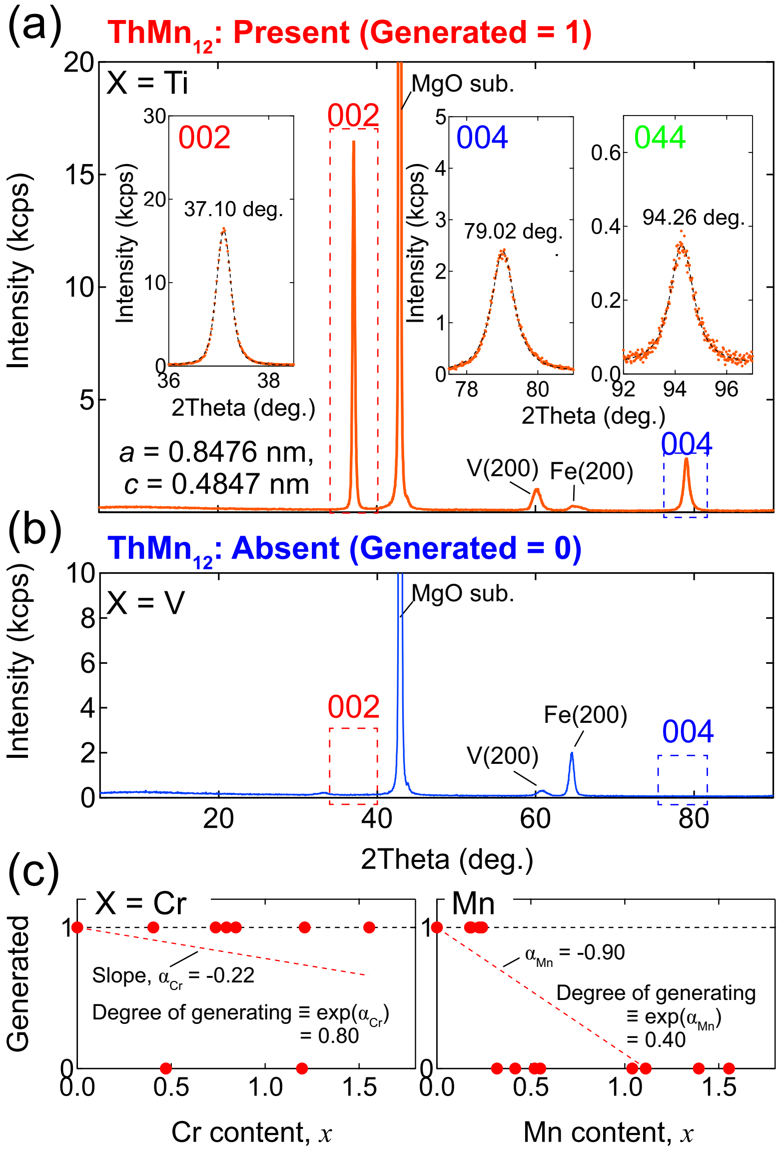

Figure 3.: (a) XRD pattern (out-of-plane) of SmFeTi thin film (Sample No. 1), showing peaks corresponding to the (002) and (004) planes of the $ThMn_{12}$ structure. The inset highlights the (044) peak obtained through fine angular adjustment. (b) XRD pattern of SmFeV thin film (Sample No. 15), showing no peaks corresponding to the $ThMn_{12}$ structure. (c) Quantification of $ThMn_{12}$ phase formation expressed as the "Degree of Generating," defined by $\exp(\alpha)$ from a linear fit of Generated versus x (additive concentration), for T=Cr,Mn.

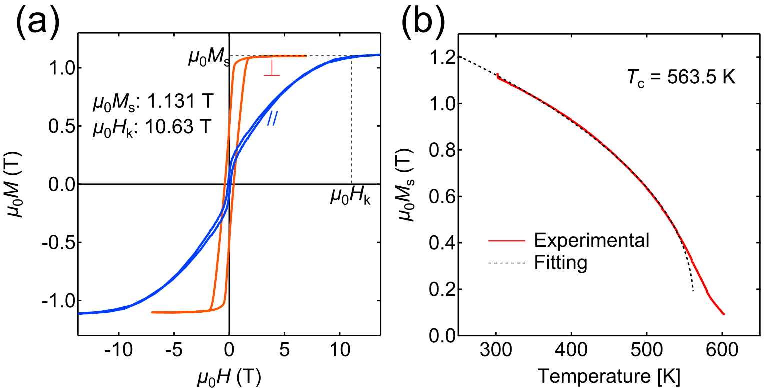

Figure 4.: (a) Magnetic hysteresis loops of SmFeTi thin film (Sample No. 1) measured with magnetic field directions both perpendicular and parallel to the film plane. (b) Magnetization as a function of temperature for SmFeTi thin film (Sample No. 1).

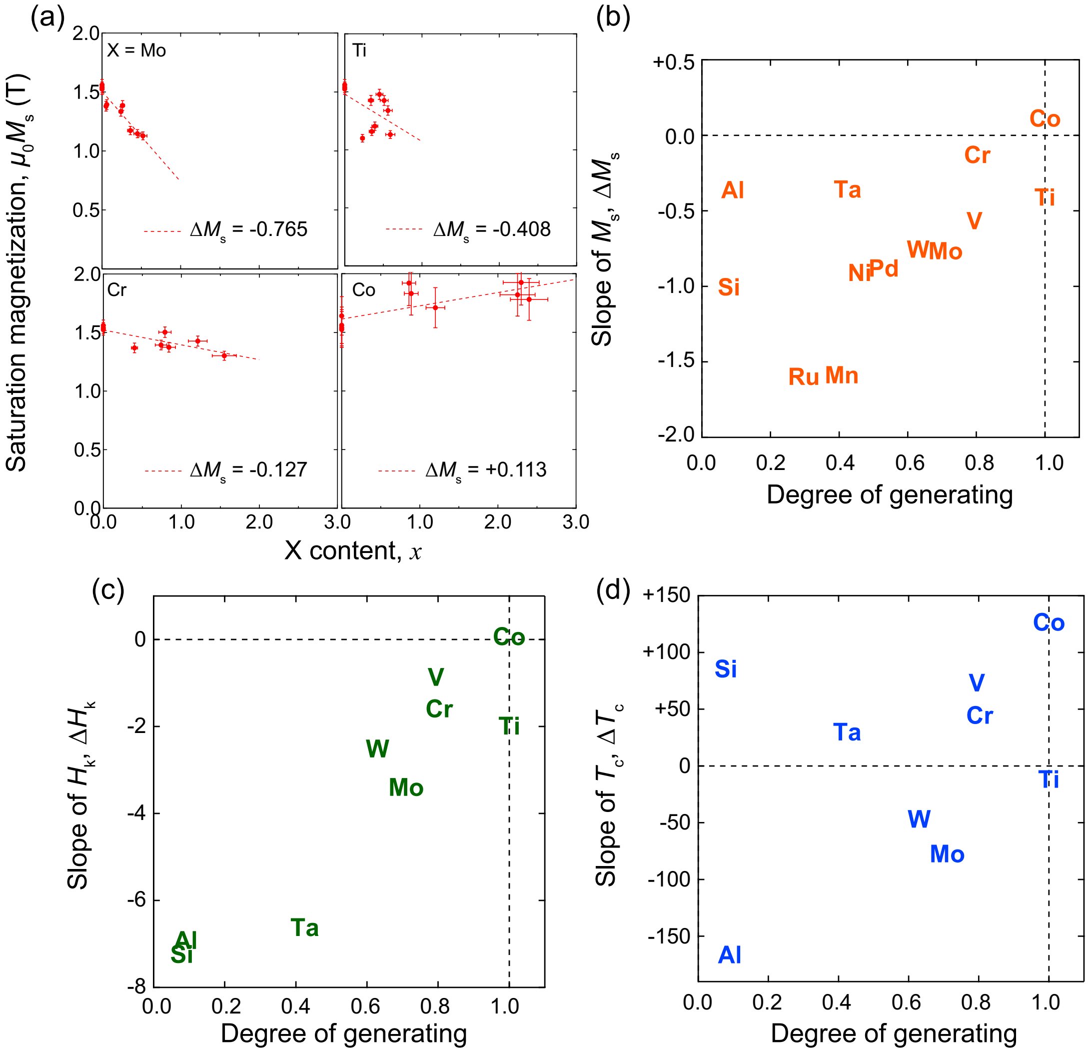

Figure 5.: (a) Saturation magnetization $\mu_0 M_s$ as a function of additive concentration x for $T =$ Mo, Ti, Cr, and Co, with literature values for Co included for comparison [37–39]. (b) Relationship between ΔM_s and the Degree of Generating. (c) Relationship between ΔH_k and the Degree of Generating for various additives. (d) Relationship between ΔT_c and the Degree of Generating.

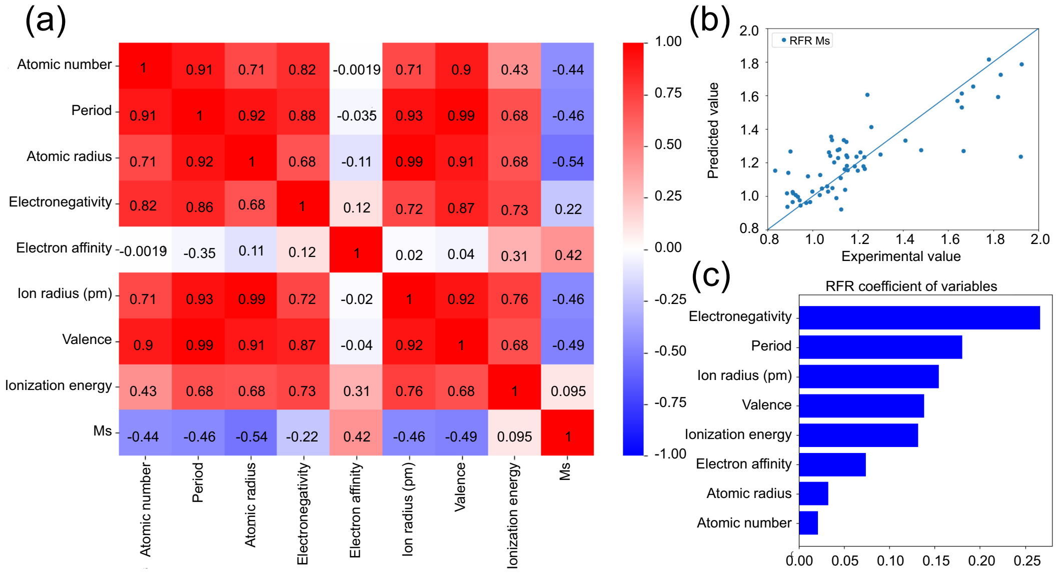

	Atomic number	Period	Atomic radius	Electronegativity	Electron affinity	Ion radius (pm)	Valence	Ionization energy	Ms
Atomic number	1	0.91	0.71	0.82	-0.0019	0.71	0.9	0.43	-0.44
Period	0.91	1	0.92	0.88	-0.035	0.93	0.99	0.68	-0.46
Atomic radius	0.71	0.92	1	0.68	-0.11	0.99	0.91	0.68	-0.54
Electronegativity	0.82	0.86	0.68	1	0.12	0.72	0.87	0.73	0.22
Electron affinity	-0.0019	-0.35	0.11	0.12	1	0.02	0.04	0.31	0.42
Ion radius (pm)	0.71	0.93	0.99	0.72	-0.02	1	0.92	0.76	-0.46
Valence	0.9	0.99	0.91	0.87	-0.04	0.92	1	0.68	-0.49
Ionization energy	0.43	0.68	0.68	0.73	0.31	0.76	0.68	1	0.095
Ms	-0.44	-0.46	-0.54	-0.22	0.42	-0.46	-0.49	0.095	1

Figure 6.: (a) Heatmap of Pearson correlation coefficients showing the strength and direction of linear relationships between the descriptors (Atomic number, Period, Atomic radius, Electronegativity, Electron affinity, Ion radius, Valence, and Ionization energy) and the target variable $\mu_0 M_s$ in the 5th Random Forest Regression analysis.
(b) Scatter plot of experimental versus predicted $\mu_0 M_s$ values. (c) Feature importance parameters estimated via cross-validation using the trained model.

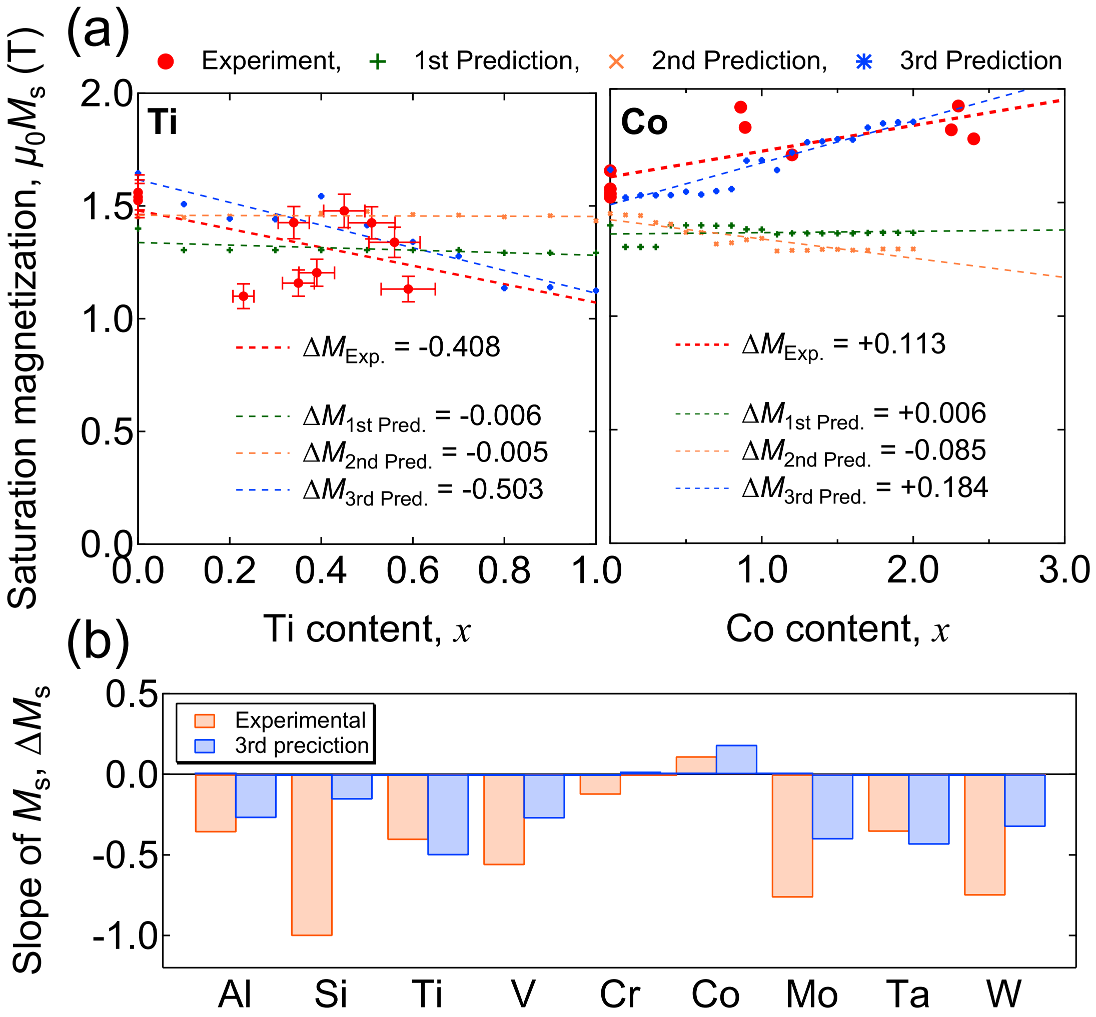

Figure 7.: (a) Comparison of experimental and predicted saturation magnetization ($\mu_0 M_s$) for T = Ti and Co as a function of additive element concentration (horizontal axis). The predictions are derived from the 1st, 2nd, and 3rd trials. (b) Comparison of ΔM_{exp} for each additive element with $\Delta M_{3rdpred.}$ from the third analysis.

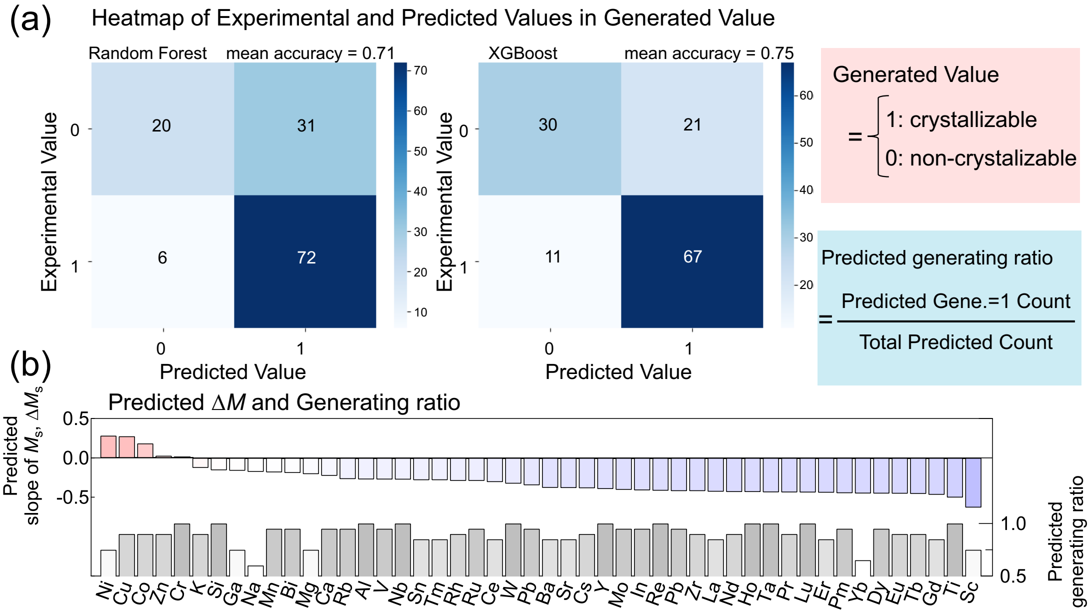

Figure 8.: (a) Heatmaps comparing experimental and predicted Generated values using Random Forest and XGBoost algorithms. Mean accuracies of 0.71 (Random Forest) and 0.75 (XGBoost) demonstrate the utility of the machine learning approach. (b) Plot of $\Delta M_{3rdpred.}$ values for all explored elements versus their predicted generating ratios, arranged in descending order of $\Delta M3rdpred.$.